Nanotechnology

PAPER

Modeling nanoscale temperature gradients and conductivity evolution in pulsed light sintering of silver nanowire networks

IOP Publishing Nanotechnology
Nanotechnology 29 (2018) 505205 (15pp) https://doi.org/10.1088/1361-6528/aae368

Modeling nanoscale temperature gradients and conductivity evolution in pulsed light sintering of silver nanowire networks

Michael Dexter[1], Andrew Pfau[2], Zhongwei Gao[2], Gregory S Herman[2], Chih-hung Chang[2] and Rajiv Malhotra[1]

[1] Department of Mechanical and Aerospace Engineering, Rutgers University, Piscataway, New Jersey, United States of America
[2] School of Chemical, Biological and Environmental Engineering, Oregon State University, Corvallis, Oregon, United States of America

E-mail: rajiv.malhotra@rutgers.edu

Received 15 June 2018, revised 16 September 2018
Accepted for publication 21 September 2018
Published 12 October 2018

Abstract

Sintering of metal nanowire (NW) networks on transparent polymers is an emerging approach for fabricating transparent conductive electrodes used in multiple devices. Pulsed light sintering is a scalable sintering process in which large-area, broad-spectrum xenon lamp light causes rapid NW fusion to increase network conductivity, while embedding the NWs in the polymer to increase mechanical robustness. This paper develops a multiphysical approach for predicting evolution of conductivity, NW fusion and nanoscale temperature gradients on the substrate during pulsed light sintering of silver NWs on polycarbonate. Model predictions are successfully validated against experimentally measured temperature and electrical resistance evolution. New insight is obtained into the diameter-dependent kinetics of NW fusion and nanoscale temperature gradients on the substrate, which are difficult to obtain experimentally. These observations also lead to the understanding that NW embedding in intense pulsed light sintering (IPL) can occur below the glass transition temperature of the polymer, and to a new differential thermal expansion-based mechanism of NW embedding during IPL. These insights, and the developed model, create a framework for physics-guided choice of NWs, substrate and process parameters to control conductivity and prevent substrate damage during the process.

Supplementary material for this article is available online

Keywords: intense pulsed light sintering, transparent electrode, nanowire, multiphysical modeling

(Some figures may appear in colour only in the online journal)

1. Introduction

Electrodes based on transparent and flexible conducting films have applications in multiple devices including displays, organic light emitting diodes, photovoltaic cells, flexible heaters and wearable electronics. While indium-tin-oxide has conventionally been used as the material for such films, its brittleness and high cost have created a need to use alternative materials [1]. Metallic nanowires (NWs), e.g., silver (Ag) and copper, deposited as morphologically sparse networks on transparent and flexible polymer substrates have emerged as a potential alternative due to the high transmittance, high flexibility, and low-cost deposition of the electrode. A key requirement for such NW networks is low electrical resistance, which must be achieved rapidly over large areas for economic feasibility of the device.

One approach to achieving this is to increase the electrical percolation of the NW network by fusing the NWs at their contacts. Intense pulsed light sintering (IPL) has emerged as a process that can perform this sintering rapidly,

over a large area, and with low substrate damage [2]. IPL uses large-area (e.g., optical footprint $\geqslant$ 12 feet by 0.75 inches here) and broad-spectrum (energy distributed over 350–800 nm wavelengths) xenon lamp light to excite plasmon resonance in the NWs. This heats up the NWs locally and rapidly (e.g. in a few milliseconds in this work), leading to mass transfer and neck formation at the NW contact points within a few milliseconds over the above optical footprint. Due to its large-area and high speed sintering capacity, non-contact and ambient condition operation, and roll-to-roll compatibility [3–9] IPL has a significant advantage in terms of scalable production as compared to processes like thermal sintering, laser irradiation, electrical fusion, and vapor deposition [10].

IPL of Ag NWs on PET substrates [11] has shown that greater pulse fluence results in greater conductivity due to increased fusion at the NW contacts, provided the fluence is above a critical threshold. However, too high a fluence can also cause temperature induced substrate damage. Increasing the as-deposited areal concentration of the NWs reduces the pre-IPL resistance, but also reduces the optical transmittance of the NW network [12]. IPL can also enable embedding of the NWs into the substrate, and consequently increase mechanical robustness and adhesion, without any complex chemical or coating processes [2, 13, 14]. A typically proposed mechanism for NW embedding into the polymer during IPL is that the local substrate temperature exceeds its glass transition temperature, resulting in encapsulation of the NWs by the softer polymer [2].

Currently, the choice of IPL parameters that prevent substrate damage while achieving the desired conductivity is performed via experimental iterations for each combination of NW material, NW diameter, NW areal concentration, and substrate material. There is a need to develop modeling approaches that can provide insight into the evolution of temperatures and electrical resistance during the process. This is critical for enabling physics-based choice of NW properties, substrate material and IPL parameters. Multiple theoretical efforts have focused on predicting temperature evolution during IPL of morphologically dense nanoparticle-based films [15–19]. In comparison, there have been relatively fewer theoretical efforts on IPL of morphologically sparse NW networks. An effective medium based thermal model with certain parameters of Ag NW network thickness and density was used to predict peak temperature rise during IPL [20]. However, the authors noted that the predicted temperatures would be significantly higher with this approach since the highly porous nature of the NW network and the consequently significant deviation in thermal behavior from a solid film not considered [13]. To account for this discrepancy, since SEM showed that 20% of the area of the substrate was covered by the NWs in experiments, the authors assumed that the temperature was scaled by 20% of the predicted temperature rise. An electromagnetic model [10] was also developed to capture localized heat generation in a NW on a polymer substrate, but this analysis was not extended to predicting temperature evolution and sintering in the NW network.

Due to the significant difference in thermal properties of the metal NWs and the polymer substrates, high temperature gradients on the substrate are expected during IPL. Experimental temperature measurement during IPL, with the nanoscale resolution required to uncover these gradients, is quite difficult and modeling may provide further insight. However, the above modeling approaches do not account for randomness in NW orientation and since nanoscale thermal analysis is not performed the local temperatures in the polymer substrate cannot be obtained. Further, these approaches do not model NW fusion and subsequent change in resistance since the thermal models are not linked to models of neck growth between the NWs. Neck growth due to atomic diffusion between NWs can be modeled using molecular dynamics (MD) simulations [21]. However, the time scales involved in IPL (milliseconds of on-time and off-time) are too long to directly use MD for modeling NW fusion during IPL. Semi-analytical models of sintering between spherical nanoparticles have been developed [22] that can potentially be linked to thermal analysis of IPL, but need to be informed by size- and shape-specific diffusion coefficients to predict realistic nanoscale neck growth between NWs. Such MD-informed analytical models of solid-state neck growth between NWs have not yet been explored ort been linked to the temperature and resistance evolution during IPL of metal NW networks.

Physically, neck growth at the NW contacts during IPL results in a reduction in NW network resistance. This neck growth is due to atomic mass transfer at the NW contacts and is governed by the temperature history of the NWs during IPL (since external pressure is absent in the process). The NW temperature evolution is in turn driven by the absorption of xenon light and governed by the nanoscale heat transfer between the NWs, the substrate and the environment. Further, predicting substrate temperatures is critical to controlling substrate damage. Capturing this multiphysical nature of IPL, spanning from atomic mass diffusion at NW interfaces to nanoscale optical absorption and thermal transport to mesoscale conductivity evolution, is critical to physically reasonable modeling of the process.

The goal of this paper is to develop a modeling framework which uses the NW material, NW diameter, and the optical absorption of the as-deposited NW network in the energetic spectrum of the xenon lamp, to predict the change in sheet resistance as a function of the IPL parameters. The above inputs are usually determined easily, as shown in the experimental portion of this paper. In this work, experiments are performed to record the in-process temperature evolution, electrical resistance, optical properties and NW network morphology as a function of varying pulse fluence during IPL of Ag NW networks on polycarbonate substrates. A nanoscale thermal finite element analysis that accounts for randomness in NW orientation is used to predict temperature evolution and the predictions are successfully validated against experimentally recorded temperatures. MD simulations of fusion between NWs are performed and used to modify semi-analytical models of nanoparticle sintering for predicting neck growth at NW contacts as a function of the temperature history. This extended sintering model is then used in conjunction with temperature predictions from thermal analysis, and a

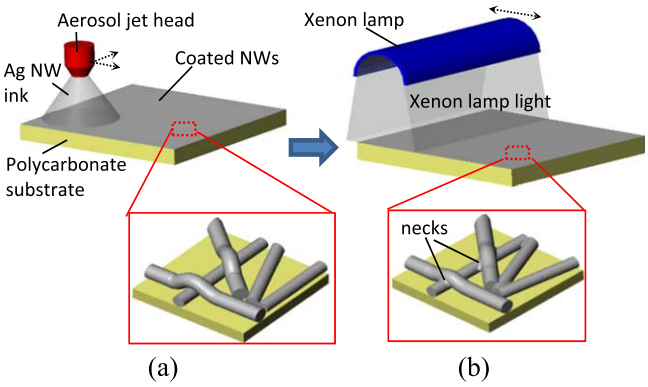

Figure 1. Schematic of (a) aerosol-jet deposition of NW-inks (b) IPL of deposited NW network.

thermodynamics-based analytical model of neck-size-dependent electrical resistance, to predict the change in sheet resistance of the NW network as a function of IPL fluence. The sheet resistance predictions are successfully validated against experimentally measured change in sheet resistance after IPL. The obtained nanoscale view of temperature evolution provides insight into temperature gradients on the polymer substrate and leads us to a new mechanism of NW embedding, which is difficult to obtain experimentally.

2. Methods

2.1. Experimental

Silver NWs of 50 nm nominal diameter and 100–200 μm length (ACS Materials) were suspended in ethanol at a concentration of 1 mg ml^{-1}, and aerosol-jet deposited on a 0.5 mm thick polycarbonate sheet (McMaster Carr, no surface coating) using an ultrasonic atomizing nozzle (Sonaer Inc.). This wide-area aerosol-jet nozzle was mounted on a three-axis gantry stage to control nozzle height from the substrate, travel speed of the nozzle and 2D path traversed in the plane of the substrate (figure 1(a)). The solution delivery rate, atomizer frequency and power, and nozzle air pressure were additional controllable parameters. IPL was performed using a Sinteron 3000 Xenon flash lamp (Xenon Corp.) with an elliptical reflector, during which the coated samples were placed on a moveable stage at a distance of 1.5 inches from the lamp (figure 1(b)). The stage was initially held at room temperature. The resulting optical footprint of the pulsed light at the substrate was approximately 16 inches $\times$ 1.5 inches. The xenon lamp energy spectrum, as provided by the manufacturer (figure S1 in supplementary information is available online at stacks.iop.org/NANO/29/505205/mmedia). The on-time t_{on} (in microseconds) and the lamp voltage V (in volts) are used to control the optical energy per pulse E_p according to the relationship $E_p = (V/3120)^{2.4} \times t_{on}$ as supplied by the manufacturer. The number of IPL pulses was fixed at one and lamp voltage was fixed at 2.8 kV. E_p was varied at 4, 8, 12, 14 and 16 J cm^{-2} by changing t_{on} at 680, 1355, 2030, 2365 and 2705 μs, respectively.

Thermocouples embedded into the nanomaterial film have been used in past work [16] to measure temperature evolution during IPL of dense spherical nanoparticle films. However, given the morphologically porous and optically transparent nature of the NW networks being considered here the thermocouple would suffer direct exposure and heating by the pulsed light itself. Therefore, a non-contact Micro-Epsilon TIM 200 thermal camera was used to measure evolution of surface temperature on the side of the sample facing the lamp. Sample emissivity was calibrated by heating the coated sample to 80 °C with a hotplate within the above described IPL setup and adjusting the emissivity to match the steady-state substrate temperature. Sheet resistance was measured both before and after IPL using a four-point-probe (Signatone) and a Keithley source meter. At least four separate measurements were taken to obtain an average and standard deviation in sheet resistance. The percentage optical transmissivity T and reflectivity R of the samples in a range of 300–800 nm were measured using a Jasco UV–vis Spectrophotometer. Reflectance was measured using a 60 mm integrating sphere integrated with the same instrument. The angle of incidence was approximately 5 degrees and the reference material was spectralon (99% reflectance). The corresponding percentage optical absorption A was calculated as $A = 100\text{-}T\text{–}R$.

The effect of the aerosol-jet parameters on the deposited network consistency and morphology has been extensively investigated before, e.g., [23]. Further, the effect of changing the areal NW concentration on as-deposited electrical resistance and transmittance is also well known [12]. Since the focus of this paper is on modeling the effect of the IPL parameters on resistance evolution, the aerosol-jet parameters and therefore the deposited NW area coverage were kept constant here. The aerosol-jet nozzle was programmed to travel in 10 overlapping in-plane tracks with 5 mm spacing between tracks with the frequency and power input of the ultrasonic atomizer set to 60 kHz and 8 Watts, respectively. The nozzle travel speed and nozzle height were set at 6000 mm min^{-1} and 35 mm above the substrate respectively. The solution delivery rate to the nozzle from the syringe pump was 1.5 ml min^{-1} and air pressure to the nozzle was 0.5 psi. Five coating repetitions yielded an as-deposited sheet resistance of 60 $\pm$ 8 Ω/sq.

2.2. Computational

The developed computational framework consists of the following linked components, i.e., optical absorption-based nanoscale thermal model, a modified semi-analytical model of NW sintering in turn informed by MD simulations, and a thermodynamics-based model of change in network resistance as a function of neck growth between NWs. These models are now individually described in detail.

The thermal model implemented in COMSOL FEA consists of a unit cell with individual 50 nm diameter Ag NWs with their axes along random in-plane orientations,

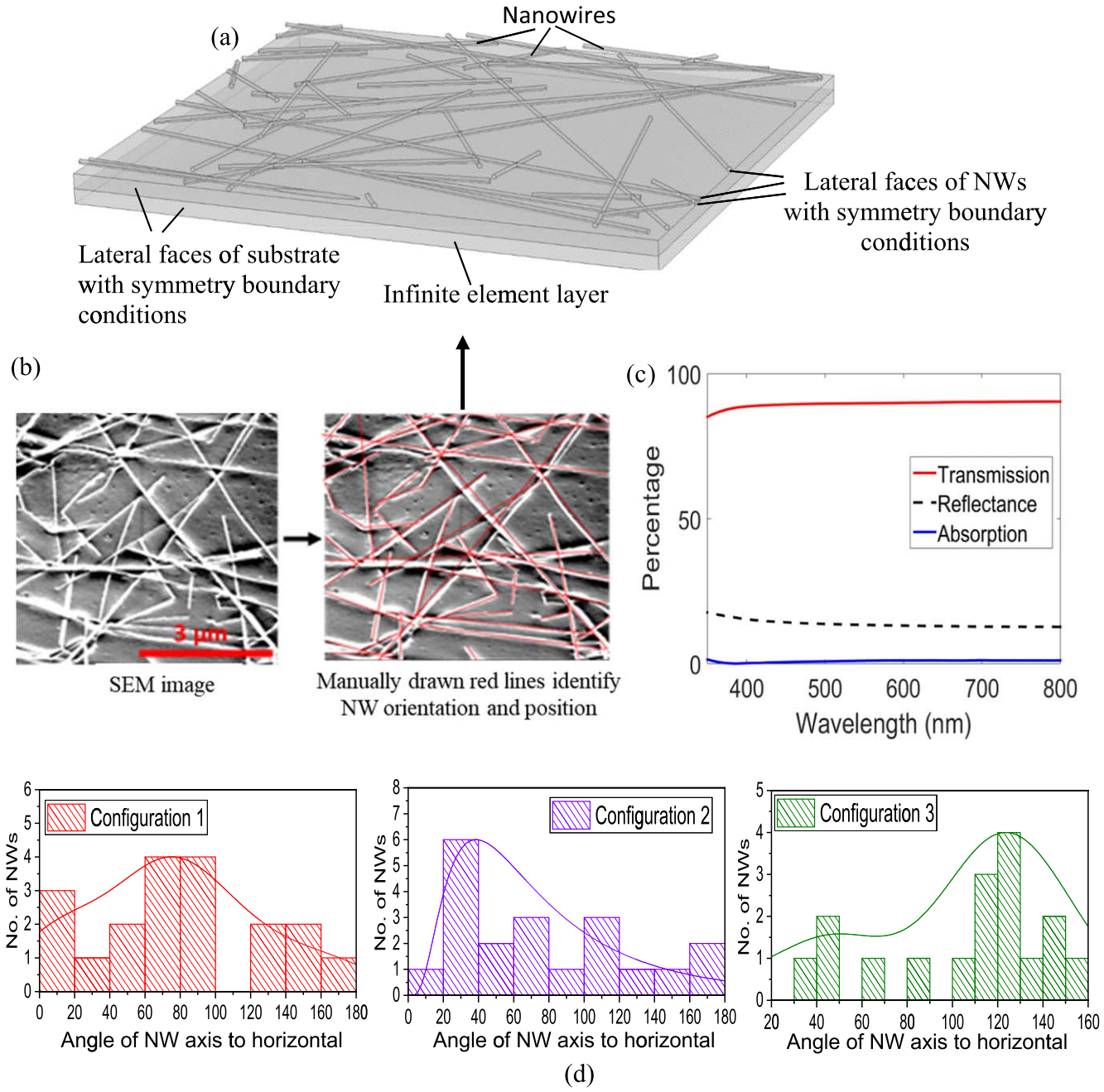

Figure 2. (a) Schematic of thermal finite element model. (b) Example of conversion of SEM image to COMSOL model. (c) Optical properties of bare polycarbonate substrate. (d) Distribution of angles that the NW axis makes to the fixed in-plane horizontal axis for the different NW configurations modeled here.

arranged in two layers on a polycarbonate substrate (figure 2(a)). This number of layers was based on SEM images from experiments, shown in section 3.1. The random axis orientations were obtained from SEM images of the as-deposited NWs and each layer contained half the total number of NWs modeled. Further, for intersecting NWs in the same layer a geometric simplification was made by combining them into a single object. An example of one such SEM image, and its conversion to a COMSOL model is shown in figure 2(b). The substrate consisted of a layer of polycarbonate meshed with regular elements, and an infinite element layer below it with a pole distance equal to the polycarbonate substrate thickness used in experiments. The bottom of the infinite element substrate layer had an insulating boundary condition as in experiments. Convective and conductive losses were allowed from both the NWs and the substrate. Table 1 shows the corresponding thermal properties of silver and polycarbonate and the convective loss coefficient. While the thermal conductivity of metals like silver is known to be dependent on the NW diameter [24] and is specified as that of bulk silver here, it has no significant effect on temperature evolution based on the consideration that the NW network has a Biot number much lesser than 1, as will be explained shortly.

Table 1. Thermal properties used in FEA.

Property	Silver	Polycarbonate
Thermal conductivity ($W\,m^{-1}\,K^{-1}$)	406	0.25
Density ($g\,cm^{-3}$)	10.5	1.20
Specific heat capacity ($KJ\,kg^{-1}\,K^{-1}$)	0.23	1.25
Convective loss coefficient ($W\,m^{-2}\,K^{-1}$)	10	

Symmetry boundary conditions were used at the lateral NW and substrate surfaces, as shown in figure 2(a). This ensured that no heat left or entered the system by specifying that $\mathbf{n}.\mathbf{q} = 0$, where $\mathbf{n}$ is the normal to the face and $\mathbf{q}$ is the heat flux. Intuitively, this mirrors the unit cell geometry about the four lateral symmetry planes by saying that the temperature gradient across the plane is zero, thus capturing the fact that the in-plane size of the substrate and the NW length is larger than in the modeled unit cell.

To converge on the size of the unit cell the length of the square unit cell was changed from 12, 8, 5 and 3 μm over the same SEM image for fluence $4\,J\,cm^{-2}$. These thermal simulations were performed for three SEM images each from the center, left side and right side of the sample, e.g., figures S2(a)–(c) in supplementary information. Representative temperature contours for these different sized unit cells are shown in figures S2(d)–(e) (supplementary information). The average substrate temperatures at the end of the optical pulse were found to be very similar irrespective of the location at which SEM images were taken (figures S2(f)–(h) in supplementary information). Thus, the long-range order of the NWs did not affect short range results significantly and a unit cell size of 3 μm × 3 μm was used as sufficient to model the temperatures. Three distinct geometric configurations of NWs (for unit cell size 3 μm × 3 μm) were used for distinct thermal simulations for each pulse fluence. In these unit cells the NWs covered 22%, 24% and 27% of the substrate area, very close to that in experiments (25%). The wide distribution of the NW orientation angles to the fixed horizontal axis and the significant difference in the skewness of the distribution from one configuration to another (figure 2(d)) captured a significant variation in the NW orientation. At the same time, modeling individual NWs ensured that nanoscale temperature gradients on the polymer around the NWs were captured.

Since the bare polycarbonate substrate had very low optical absorption (nearly 0%, figure 2(c)) in the energetic spectrum of the xenon lamp, the thermal power Q driving the temperature rise during IPL arose almost entirely from absorption by the NWs as shown in equation (1). Here F is the cumulative power output from the xenon lamp (equation (2)), P is the constant total power input into the lamp, λ is the optical wavelength, $X(\lambda)$ is the fractional power spectrum of the xenon lamp as supplied by the manufacturer and $A(\lambda)$ is the fractional optical absorption of as-deposited samples within the energetic spectrum of the xenon lamp. $A(\lambda)$ was obtained by subtracting the absorption of the bare polycarbonate (figure 2(c)) from that of the NW network (shown later in results section), thus accounting for the the difference in the optical properties of the substrate and the NWs. Based on the known optical footprint of the lamp light at the substrate a_{lamp} and the known in-plane area of the NW domains in the thermal simulation a_{sim}, the total thermal power in thermal simulations was specified as $Q \times a_{sim}/a_{lamp}$. Due to the relatively high inherent thermal conductivity of silver even while accounting for NW size effects, the high surface area to volume ratio of the NWs, and the high degree of porosity in the network, the Biot number of the NW network is less than 1. Therefore, the role of thermal conductivity and temperature gradients in the NW network itself is negligible and the total thermal power was applied as a uniformly distributed heat source to the NW domain. We note that since the measured $A(\lambda)$ is an average field response this heat source (i.e., $Q \times a_{sim}/a_{lamp}$) was applied a total heat source to the entire NW assembly rather than to each NW

$$Q = \frac{F\sum_{350\text{ nm}}^{800\text{ nm}} A(\lambda).\,X(\lambda)}{\sum_{350\text{ nm}}^{800\text{ nm}} X(\lambda)}, \tag{1}$$

$$F = P\sum_{350\text{ nm}}^{800\text{ nm}} X(\lambda). \tag{2}$$

We note that the local orientations of the individual NWs with respect to the electric field polarization can produce spatially different heat flux. However, the resulting temperature gradients in the NW network itself are ignored here since they are expected to equilibrate out very quickly due to a low Biot number. Via the above prescription of the heat source based on the low Biot number we effectively treat the NW network as a thin film consisting of NW ligaments with explicitly modeled porosities, while avoiding the use of effective thermal models that cannot account for such high porosities. The ability of this thermal model to predict the experimentally measured temperatures is a key measure of the feasibility of the above model, and is discussed in the results section.

An analytical model of sintering between spherical nanoparticles after [22] was modified to model neck growth between NWs as a function of their predicted temperature history. This model is based on an energy and mass balance during sintering in the presence of externally applied forces and temperature rise as a function of time. In the absence of external mechanical forces (as in IPL) the rate equation for evolution of neck radius x is expressed in terms of NW radius R, diffusion parameter D, surface energy per unit area γ and the dihedral angle ψ as

$$\dot{x} = \frac{8RD\gamma}{x^5}\left[4R\left(1 - \cos\frac{\psi}{2}\right) + x\sin\frac{\psi}{2}\right]. \tag{3}$$

The diffusion parameter is given by $D = D_f\,\delta_f\,\Omega/kT$ where D_f is the effective atomic diffusion coefficient between the NWs, δ_f is the thickness of the region in which atomic diffusion is active (0.5 nm here, [25]), Ω is the atomic volume of silver ($10.27\,cm^3\,mol^{-1}$ here, [26]), k is Boltzmann's constant and T is the temperature. The temperature dependent diffusion coefficient was captured in an Arrhenius form using a pre-exponential factor D_0 and an activation energy term E_a as $D_f = D_o\,e^{(-Ea/kT)}$. The pre-exponential factor is essentially the diffusion coefficient at

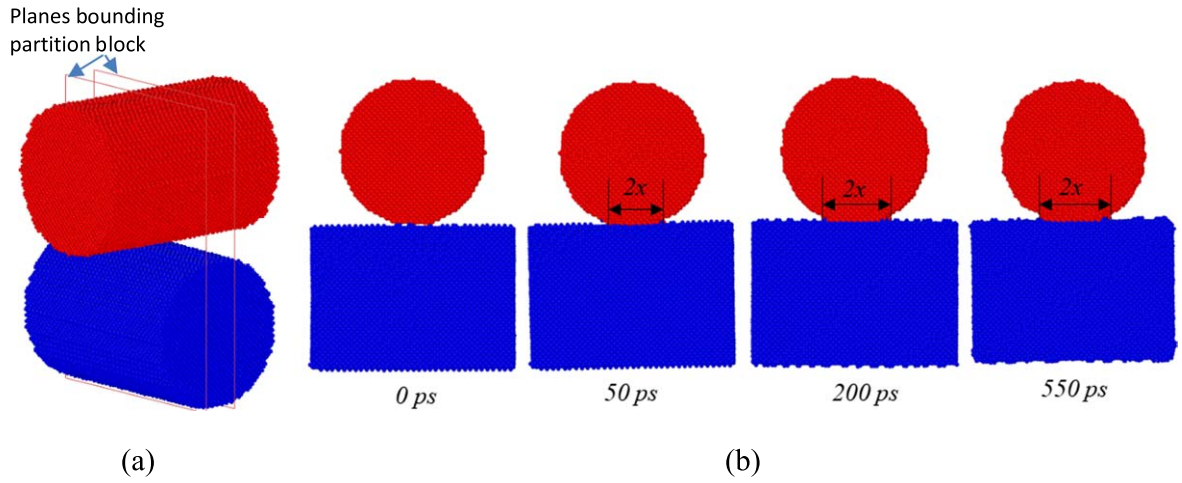

Figure 3. Snapshots from molecular dynamics simulations showing (a) setup of NW sintering simulation and bounding planes for dynamic partition block used in post-processing (b) neck radius x at different times during the simulation. Shown here for 20 nm diameter Ag NWs.

infinite temperature. Here, the dihedral angle was fixed at 179° to capture neck growth till $x/R \approx 0.95$. The specific surface energy γ was 7.1 J m^{-2} [27].

To adapt the above model for predicting evolution of neck radius x between sintering NWs, MD simulations were performed to obtain NW size-dependent D_0 and E_a for two NWs with orthogonal axes lying on top of each other (figure 3(a)). The goal was not to directly simulate the heating of the NWs during IPL, but to obtain effective diffusion coefficients for the above analytical sintering model. MD simulations were performed on the LAMMPS platform using the embedded-atom-method [28] with temperature control and with no external pressure applied. The temperature was controlled using a Nose–Hoover thermostat. No heat loss to the environment was considered. In this method the total energy of an atom E_{tot} is calculated using a pairwise energy function $V_{ij}(r_{ij})$ between atoms i and j, where r_{ij} is the distance between atoms i and j, and an atom embedded energy $F_i(\rho_i)$ where ρ_i is the electron density. The total energy of the model is the summation of that of all atoms of the system. The function parameters for silver were obtained from past work [29]

$$E_{tot} = \frac{1}{2}\sum_{ij} V_{ij}(r_{ij}) + \sum_{i} F_i(\rho_i). \quad (4)$$

The NWs were initially placed 0.1 nm apart, equilibrated for 50 ps at a temperature of 300 K, and then subjected to a temperature ramp. NWs with diameter 10, 12, 15, 20 nm were subjected to a temperature ramp of 300–900 K in 500 ps. Larger NWs of 25, 30 and 35 nm diameter were subjected to a higher temperature ramp of 300–1200 K in 150 ps to ensure that the size-dependent trends for neck growth were not observed from only a single temperature ramp. The MD-simulated and prescribed temperature profiles were found to match well (figure S3, supplementary information). The length of each NW was fixed at 2.5 times its diameter to sufficiently capture the potential contribution of atomic diffusion along the NW length to neck growth, while reducing the computational time needed. Each simulation was performed in the canonical ensemble (NVT) with an integration time step of 1 fs, temperature stabilization at every 5 fs, and the use of non-periodic boundary conditions to isolate the NWs. The evolution of neck radius during the temperature ramp in MD simulations was measured in the OVITO post-processing software by creating a 4 nm thick dynamic partition block region at the NW interface (figure 3(a)). Figure 3(b) shows the resulting cross section from which x is obtained at different points of time during the MD simulation.

We observe here that the ability of this MD geometry to capture neck growth in the NW network is based on the simplifying assumptions that the relative orientation of the NW axis has little influence on neck growth, and that contact between adjacent NWs occurs primarily as shown in figure 3(a). We note that although no dispersant was used in the experiments performed here, a dispersant on the NWs may increase the activation energy of sintering and thus reduce the sintering tendency of the NWs if it is not completely removed by the temperature induced by IPL.

The Riemann–Weber formulation (equation (5), [30]) was used to model the electrical resistance at the NW contacts as a function of neck radius x. Here, R_p is the effective electrical resistance of a NW pair and R_{solid} is the electrical resistance of the bulk material ($1.59 \times 10^{-8}\,\Omega\,$m for Ag here). Generally, the electrical resistance of an ensemble of spherical conductive particles undergoing sintering depends on the neck growth between the particles and on an electrical percolation factor [31], which is dependent on the connectivity between the nanomaterials. Therefore, here the sheet resistance of the NW network can be approximated as $K_{perc} \times R_p$ where K_{perc} is a percolation factor. During sintering of such spherical nanoparticle ensembles, K_{perc} can change due to dynamic changes in contact points between distinct nanoparticles undergoing fusion. In sparse NW networks such as the one being investigated here it is unlikely that K_{perc} changes significantly since new contact points between NWs are rarely created. Therefore, K_{perc} was assumed to be a constant here. We denote the change in sheet resistance after IPL as $\Delta R = R_0 – R$, where R_0 and R are the sheet resistance of as-deposited and post-IPL NW network.

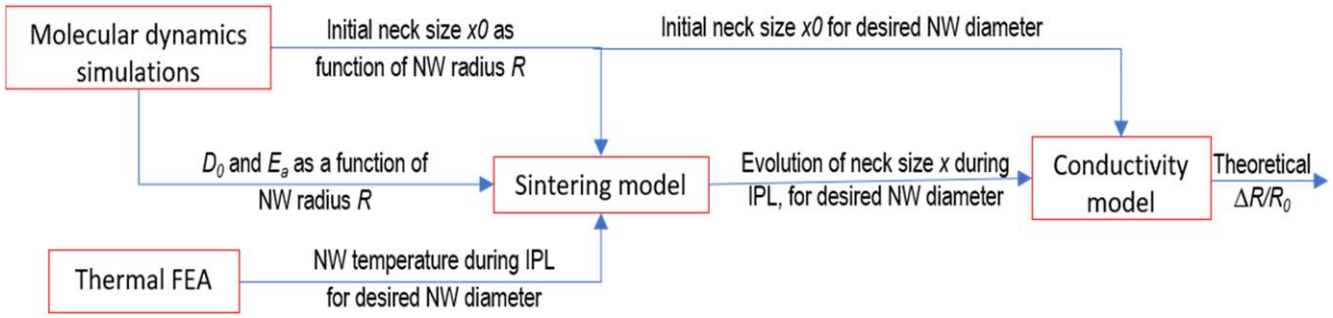

Figure 4. Schematic of interaction between models.

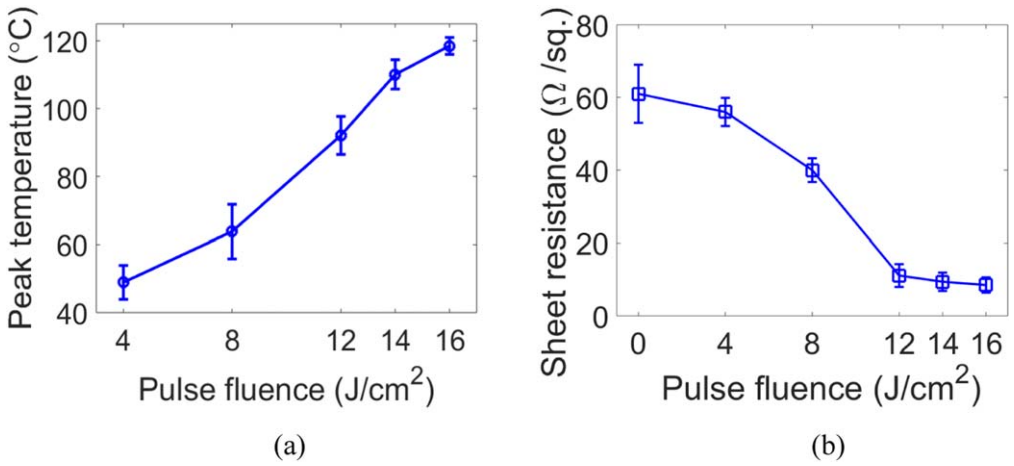

Figure 5. (a) Peak temperature during IPL as a function of the pulse fluence (b) sheet resistance as a function of the pulse fluence. 0 J cm^{-2} indicates as-deposited NW network.

Since K_{perc} is constant the normalized change in sheet resistance $\Delta R/R_0$ is obtained from equation (6), where R_{p_x} and R_{p_x0} are the predicted R_p of a NW pair at neck radius x and at initial neck radius $x0$, respectively. Since K_{perc} is assumed constant due to the sparsity of the NW network the expression in equation (6) is agnostic of the percolation model, which is why a specific percolation model is not mentioned here. The initial neck radius $x0$ between the NWs corresponds to a small neck growth that can occur between nanomaterials due to adhesive forces even at room temperature [32].

$$R_p = R_{solid}\left(\frac{R}{x} + \frac{1}{\pi}\ln\frac{2R}{x}\right), \tag{5}$$

$$\frac{\Delta R}{R_0} = 1 - \frac{R_{p\_x}}{R_{p\_x0}} = 1 - \left(\frac{\frac{R}{x} + \frac{1}{\pi}\ln\frac{2R}{x}}{\frac{R}{x0} + \frac{1}{\pi}\ln\frac{2R}{x0}}\right). \tag{6}$$

Figure 4 shows how the above described models are linked. For each NW diameter, the D_0 and E_a in the analytical sintering model were manually iterated to find a best-fit between evolution of neck radius x predicted by MD and that predicted by equation (3) for the same temperature ramps. The trends of D_0 and E_a as a function of NW diameter were fitted to polynomial best-fit curves to find D_0 and E_a for the 50 nm NW diameter case corresponding to experiments. The initial neck radius $x0$ between adjacent NWs was obtained as the neck radius at the end of the equilibration phase in the MD simulations, and then correlated to the NW diameter to find $x0$ for 50 nm diameter NWs. The temperature evolution of the 50 nm diameter NWs from thermal FEA, along with the above derived diffusion parameters and initial neck radius, was used to compute the evolution of x via numerical integration of equation (3). Then, the theoretical $\Delta R/R_0$ was calculated using the conductivity model (equation (6)).

3. Results and discussion

3.1. Experimental

The peak temperature (averaged over multiple experiments) shows a nearly linear dependence on the IPL fluence (figure 5(a)). Representative examples of measured temperature evolution for different IPL pulse fluences are provided in figure S4 (supplementary information). The peak temperature measured does not exceed the glass transition temperature of the polycarbonate, which was measured to be 153 °C using differential scanning calorimetry.

As described in the experimental methods section, the temperature measurement in this work is via detection of infrared radiation emitted by both the NWs and by the surface of the polycarbonate. Analysis of SEM images of the

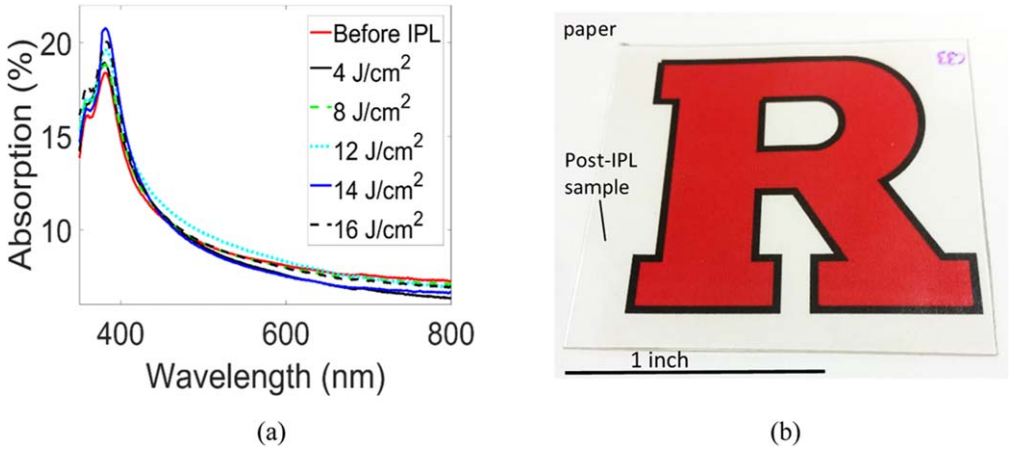

Figure 6. (a) Optical absorption, before and after IPL. (b) Image illustrating optical transmission of the NW network with the Rutgers University logo clearly visible through the post-IPL NW sample (14 J cm^{-2} pulse fluence).

as-deposited NWs showed that the NWs cover only 25% of the area of the polycarbonate (e.g. figure 2(b)). Along with this observation, the fact that the radiative emissivity of polycarbonate (≈0.9) is significantly greater than that of silver (typically ≈ 0.02–0.05) implies that most of the thermal energy received by the infrared camera was from the polycarbonate substrate. Therefore, the temperature measured by the thermal camera was closer to the average temperature of the substrate than to the NW temperature. The observed reduction in sheet resistance with increasing pulse fluence is shown in figure 5(b). At low fluence (4 J cm^{-2}) there is a negligible change in resistance, whereas the reduction is significant at 8 and 12 J cm^{-2}, indicating that these higher fluences are above the critical energy threshold needed for observable reduction in resistance. Beyond 12 J cm^{-2} the change in resistance tapers off, a phenomenon that will be explained after the computational modeling results are presented. The lowest resistance achieved is 8.5 Ω/sq. Note that each measurement shown in figure 5 was made with a freshly prepared sample.

The optical transmission at the photopic wavelength for humans (550 nm [33]) at 550 nm is 76% for unsintered samples and post-IPL samples (figure S5(a), supplementary information). This observation is similar to previous work [20], which has shown that IPL results in a negligible change in transmittance of the NW network below the damage threshold fluence. Optical reflectance spectra (figure S5(b), supplementary information) were used to obtain optical absorption of the NW network before and after IPL (figure 6(a)). Comparing these absorption curves to the nearly zero optical absorption of bare polycarbonate (figure 2(c)), we observe that the curves in figure 6(a) represent $A(\lambda)$ in equation (1). Further, since there is no appreciable change in optical absorption after IPL the total thermal power Q (equation (1)) does not change dynamically during thermal FEA. We note that the fabricated networks are still see through, as demonstrated by the clear visualization of the Rutgers university logo even when the IPL sintered sample is kept above it (figure 6(b)). SEM images of the samples, before and after IPL (figure 7) show that the NWs seem to increasingly get embedded into the polymer as the pulse energy increases. This increased NW embedding under greater IPL fluence, and a consequently greater reliability under mechanical loads has also been shown in past work [13]. Overall, the observed dependence of electrical network conductivity and the NW embedding phenomenon on pulse fluence is consistent with previous experimental observations.

3.2. Computational

Figure 8 shows contours of predicted temperature as a function of time, for pulse fluence of 16 J cm^{-2} as a representative case, and for two of the geometric configurations of NWs simulated here (additional configuration in figure S6, supplementary information). These geometric configurations of the NWs correspond to NW orientations obtained from distinct SEM images from different regions of the sample. Figures 9(a)–(e) compare the evolution of average substrate temperature obtained from FEA and averaged over three independent simulations to the measured temperature evolution, i.e., the average substrate temperature in experiments. The predicted substrate temperatures match well qualitatively with experimentally measured temperatures and have a maximum quantitative error of 10 °C–15 °C compared to experiments. Figure 9(f) compares the predicted and experimental average substrate temperature, and shows the predicted average NW temperatures, at the end of the pulse duration. The standard deviation in the predictions is based on predictions from the distinct NW configurations. The predicted peak value of average substrate temperature compares well to the experimental value (within ±7 °C) indicating that the developed FEA can predict temperature evolution in the process. The deviation in predicted temperature between different NWs, at any given time during the simulations, was less than 1 °C independent of the network's geometric configuration.

The peak value of average NW temperature is approximately 13 °C greater than the peak value of the average substrate temperature, irrespective of pulse fluence. Thus, the ratio of NW temperature to substrate temperature reduces as

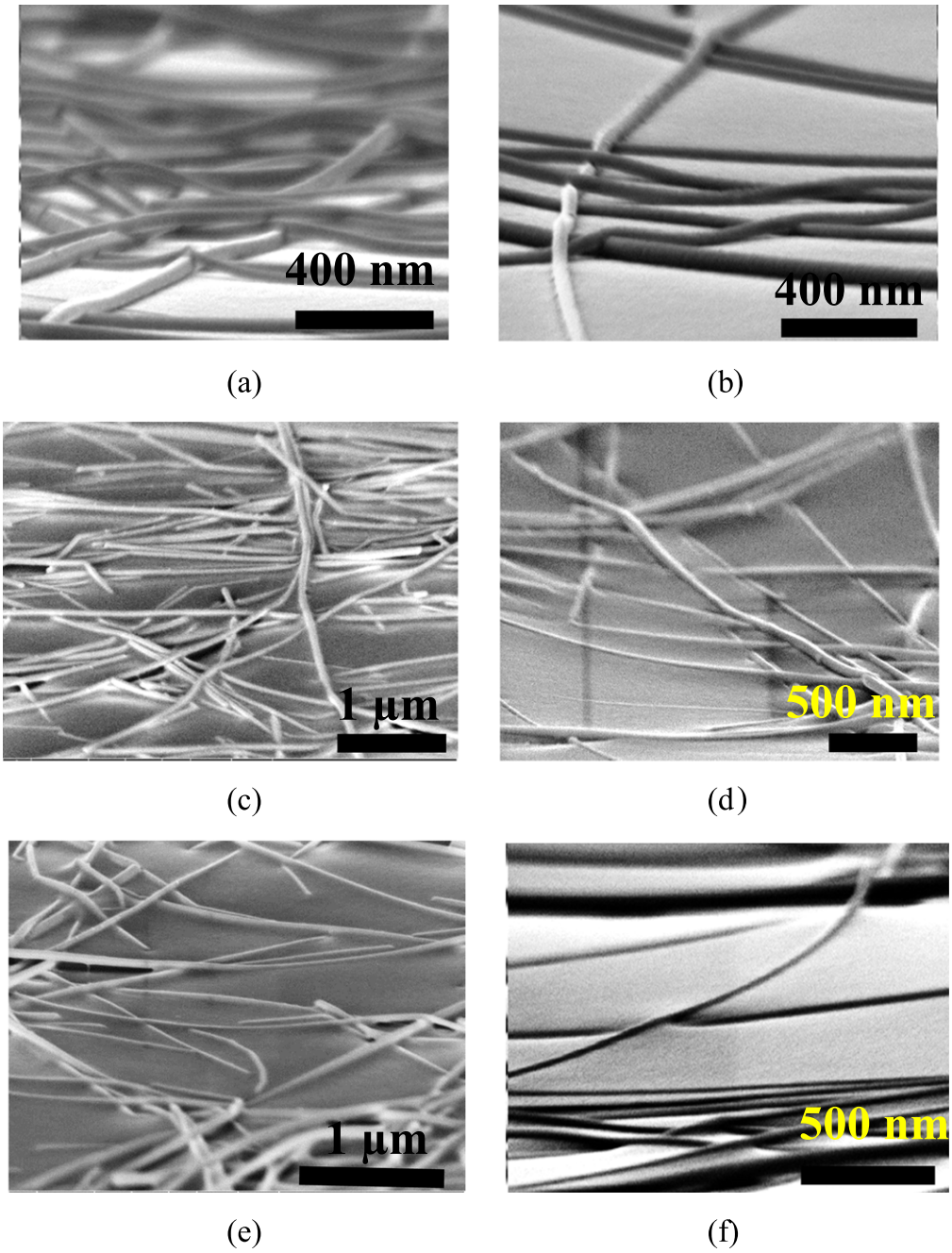

Figure 7. SEM images of (a) unsintered NW networks; and post-IPL NW networks sintered with fluence (b) 4 J cm^{-2} (c) 8 J cm^{-2} (d) 12 J cm^{-2} (e) 14 J cm^{-2} (f) 16 J cm^{-2}.

pulse fluence increases. This is because increasing pulse fluence, enabled by increasing pulse duration, results in the heat spreading out into the substrate more uniformly than at low pulse fluence. The maximum substrate temperature during IPL is expected to be at the end of the pulse duration, and for the largest pulse fluence. Figure 8 shows that the peak substrate temperature does not exceed the glass transition temperature of the polycarbonate (153 °C here). Therefore, the embedding of the NWs observed in experiments here (e.g., figure 7(f) for pulse fluence 16 J cm^{-2}) is not via softening of the polycarbonate beyond the glass transition temperature. Figure 8 also shows that during the pulse on-time a high temperature gradient is present in the polymer substrate around the NWs, both in the plane and through the thickness of the substrate. This temperature gradient has a radial pattern that expands outwards from the NW-substrate contact region with increasing on-time, with the maximum temperature in this region being the same as that of the NW. The extent of this temperature gradient does affect retention of heat by the NWs during the pulse on-time, and therefore has an indirect influence on sintering as well. Within just 0.5 ms of the pulse off-time this gradient in the substrate is reduced significantly. This is because in the absence of active optical heating the lower regions of the substrate, which are also at lower

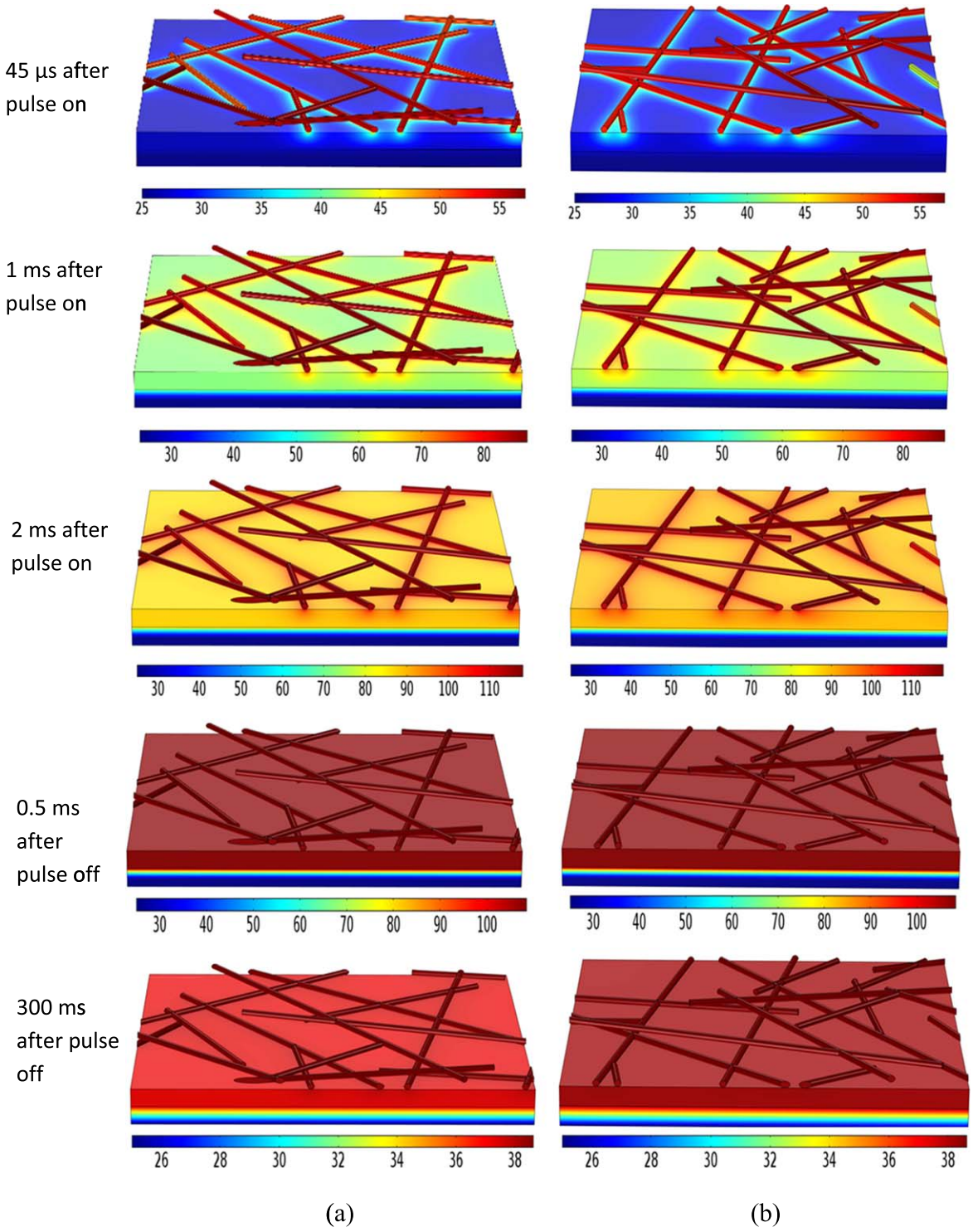

Figure 8. Temperature contours (°C) predicted by thermal FEA for the two different geometric configurations of NWs shown in (a) and (b). Shown here for 16 J cm^{-2} IPL pulse fluence.

temperature, quickly conduct heat away from the region of the substrate near the NWs.

These observations also provide an alternative hypothesis for the mechanism behind the experimentally observed NW embedding (figure 10). The typical thermal expansion coefficient of polycarbonate ($\approx$65–70 $\times$ 10^{-6} K^{-1}) is much greater than that of silver ($\approx$20 $\times$ 10^{-6} K^{-1}). The radial temperature gradient in the substrate around the NWs during the pulse on-time results in the radial region of the substrate below the NWs expanding significantly more than the silver NWs themselves, to form a local trough of polycarbonate below the NWs (figure 10(b)). Due to their weight the NWs sink into this trough. When the xenon light pulse is then turned off the resulting thermal contraction of the polycarbonate results in the NW being partly encapsulated by the polycarbonate around it (figure 10(c)), which is observed as

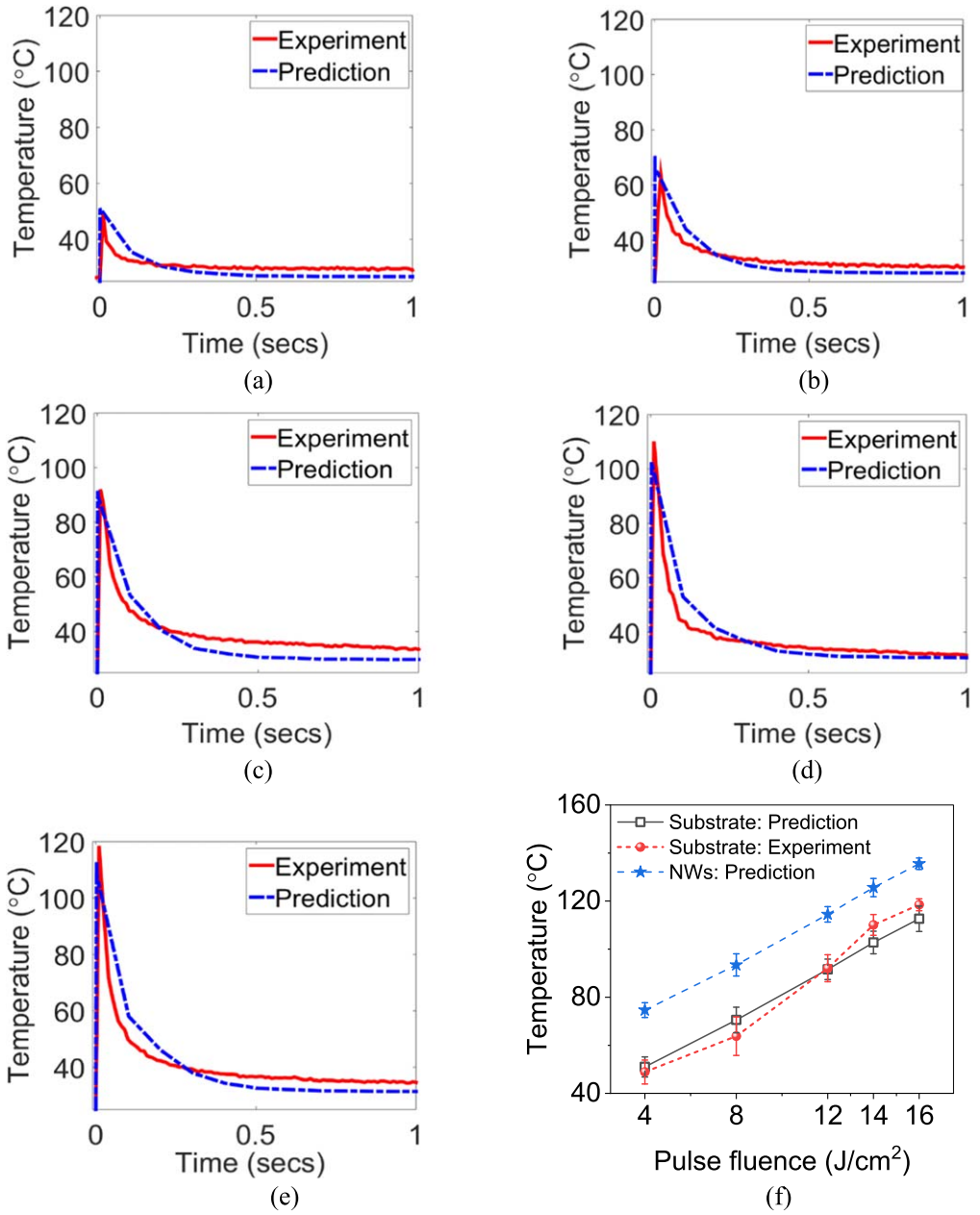

Figure 9. Comparison of predicted and experimentally measured temperature evolution for pulse fluence (a) 4 J cm^{-2} (b) 8 J cm^{-2} (c) 12 J cm^{-2} (d) 14 J cm^{-2} (e) 16 J cm^{-2}; (f) predicted and experimentally measured average temperature of substrate at the end of the pulse duration; and predicted average NW temperature at the end of the pulse duration. Standard deviations in predictions are based on results from FEA for multiple distinct NW configurations modeled here.

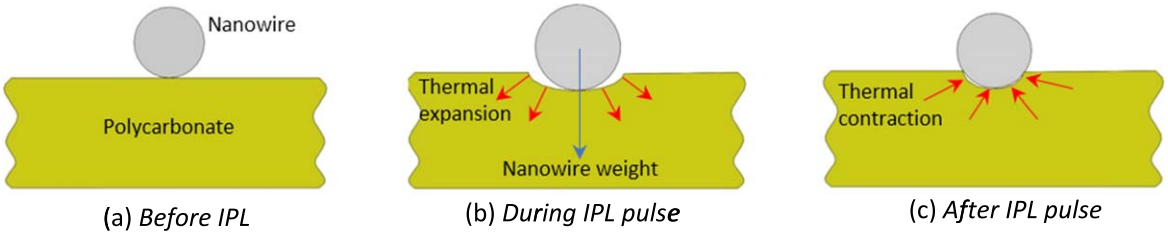

Figure 10. Schematic of proposed mechanism of NW embedding during IPL.

the NWs getting embedded into the polymer. Greater pulse energy will result in greater temperature rise and therefore greater size of trough formed, thus magnifying this effect, as is seen in our experiments and in literature [12]. This proposed mechanism might act as a complement to the glass transition based mechanism, especially when temperatures

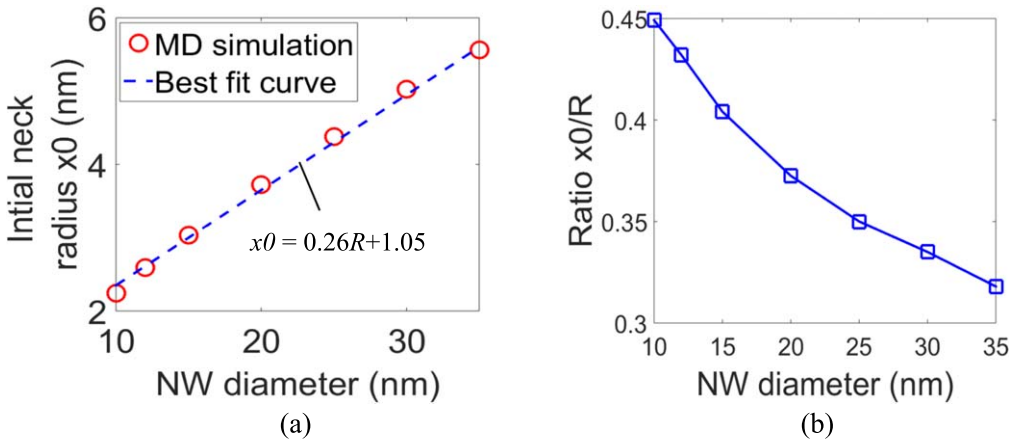

Figure 11. (a) Initial neck radius $x0$ and (b) corresponding ratio $x0/R$, predicted by MD simulations as a function of NW diameter.

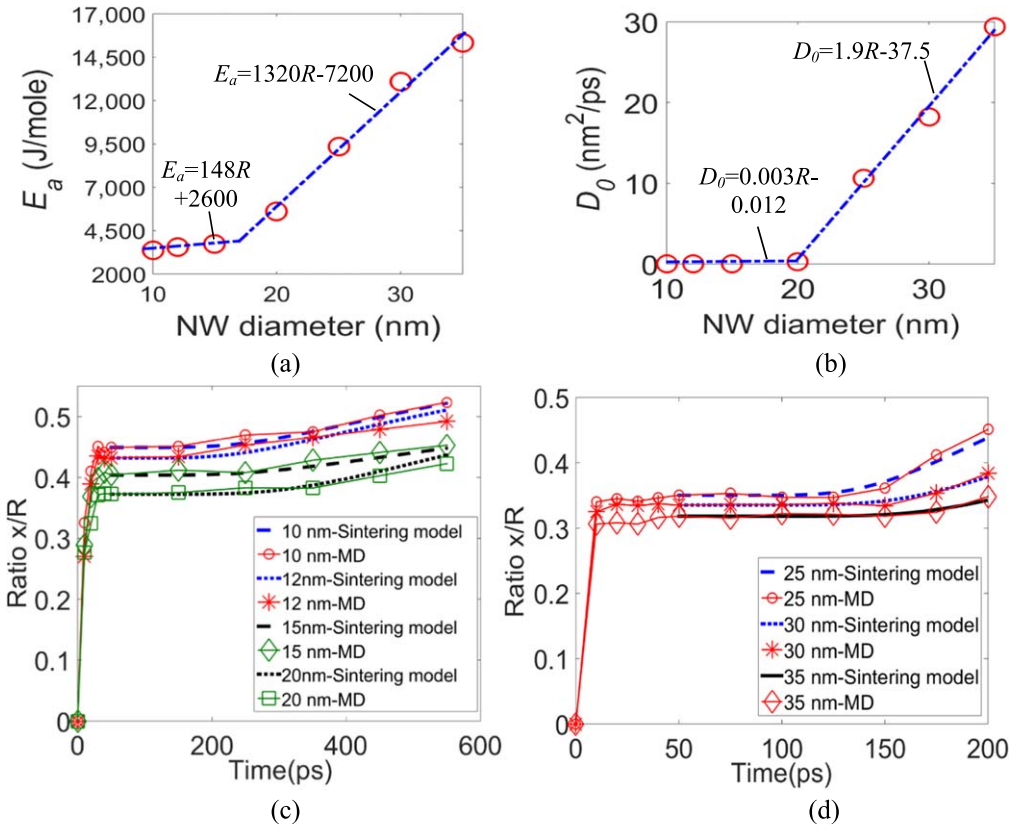

Figure 12. Correlation of (a) activation energy E_a (b) pre-exponential factor to the NW diameter, markers show data from MD simulations; comparison of x/R evolution from MD simulations and post-stabilization x/r evolution from sintering model with best-fit E_a and D_0 for (c) 10, 12, 15 and 20 nm diameter NWs (d) 25, 30, 35 nm diameter NWs. Corresponding imposed temperature ramps are mentioned in the methods section.

reach high enough for the glass transition temperature of the polymer substrate to be eventually exceeded.

The initial neck radius $x0$ (at time = 50 ps) predicted by MD simulations linearly increases with NW radius R (figure 11(a)). This relationship is used to find $x0$ for 50 nm diameter as 6.55 nm. Note that the ratio $x0/R$ which controls the resistance at room temperature decreases with increase NW radius (figure 11(b)), indicating that resistance at room temperature reduces with an increase in the NW diameter.

Figures 12(a), (b) shows the best-fit D_0 and E_a obtained by comparing the post-stabilization (time $>$ 50 ps) evolution of x/R predicted by MD to that predicted by the sintering model. The activation energy for sintering increases with greater NW diameter as per the bilinear relationship shown in figure 12(a). This is due to decreasing surface area per unit volume ratio of the NWs with an increase in diameter, which results in lesser inherent drive of the NWs to reduce surface area and therefore reduced tendency for sintering. The E_a for

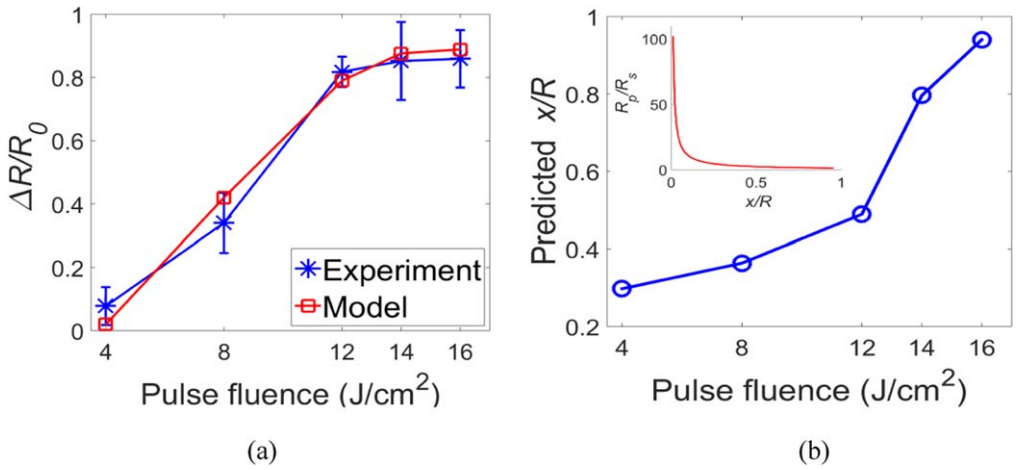

Figure 13. (a) Comparison of experimentally measured and computationally predicted change in sheet resistance as a function of pulse fluence during IPL. (b) Predicted evolution of ratio x/R during IPL, inset shows the evolution of the ratio of interparticle resistance R_p to bulk resistance R_s with the ratio x/R between two adjacent NWs undergoing sintering.

50 nm diameter NW is found as 25.8 kJ mole^{-1} using the correlation shown in figure 12(a). The D_0 for 50 nm NW diameter is similarly found to be 57.4 nm^2 ps^{-1} from figure 12(b). Figures 12(c), (d) compare the neck evolution predicted by MD to that predicted by the sintering model for the best-fit D_0 and E_a. The post-stabilization increase in x/R for the same temperature ramp reduces with greater NW diameter, from 16% to 13% for diameters for the first ramp (figure 12(c)) and from 28% to 9% for the second temperature ramp (figure 12(d)). This implies that smaller NW diameters will enable greater degree of sintering and greater reduction in resistance for the same temperature rise.

Figure 13(a) compares the predicted and experimentally measured $\Delta R/R_0$. Quantitatively, the predictions lie within the standard deviation in experimental data, indicating good predictive capability of the developed framework in terms of resistance change. The model predictions also show that $\Delta R/R_0$ tapers off beyond 12 J cm^{-2}, as is observed in experiments. It might be thought that this is because additional neck growth does not happen beyond 12 J cm^{-2} based on the assumption that a maximum sintering limit has been reached, as stated in past work on IPL of spherical nanoparticles [34]. However, the evolution of maximum x/R with pulse fluence as predicted by this validated sintering model (figure 13(b)) shows that this is not the case. The evolution of x/R does not taper off beyond the fluence of 12 J cm^{-2}, on the other hand the x/R increase substantially after this fluence value. The reason for tapering off in $\Delta R/R_0$ is more easily understood by examining the thermodynamics-based Riemann–Weber formulation (equation (5)) and observing that the ln $(2R/x)$ term results in a gradual tapering off in the change in resistance as the x/R increases (inset in figure 13(b)).

4. Conclusions

This work develops a novel multiphysics framework to predict the key product performance metric of change in electrical resistance and the key process performance metric of substrate temperatures as a function of the process parameters, NW network properties and substrate properties during IPL sintering of NW network based transparent conductive electrodes. The thermal FEA component of this framework accounts for the random orientation of the NWs in the network while using symmetry boundary conditions to emulate longer NW length than in the modeled unit cell. The sintering model accounts for NW diameter-dependent fusion by obtaining the effective diffusion coefficient as a function of the NW diameter from MD simulations. The influence of the NW diameter and area coverage of the NW network on optical absorption is incorporated by using the experimentally measured optical absorption as an input, and via the observation that IPL does not change the optical absorption significantly. This multiphysical framework is successfully validated against experimentally observed temperature evolution and normalized change in sheet resistance. The key takeaways from this work are as follows.

(1) Both temperature and resistance change are predicted well by the developed approach, despite significant assumptions and a relatively small size of the thermal unit cell. If the NW material, NW diameter and initial optical absorption of the as-deposited NW network are known then this approach can predict the change in sheet resistance after IPL. Therefore, if the as-deposited sheet resistance is known the post-IPL sheet resistance can be predicted as a function of the IPL parameters. This bridges a key gap by enabling physics-based choice of NW properties, substrate properties and IPL parameters to control the electrode's conductivity and thus take full advantage of the rapid and scalable nature of IPL.
(2) The MD simulations performed show that the kinetics of fusion between Ag NWs is significantly dependent on the NW diameter, with the rate of sintering reducing faster beyond a critical NW diameter (≈20 nm here for Ag).

This provides previously unknown insight into the kinetics of fusion of Ag NWs.

(3) The thermal FEA provides new insight into temperature gradients in the substrate during IPL and shows that the ratio of NW temperature to substrate temperature reduces with increasing pulse fluence. This is because increasing pulse fluence, via greater pulse duration, results in the heat diffusing to a greater extent into the substrate.

(4) The experimental observations, combined with the thermal model, also show that contrary to expectations in literature NW embedding in IPL can occur below the glass transition temperature of the polymer. The predicted temperature gradients in the polymer yield an alternative differential thermal expansion-based mechanism of NW embedding which can be active even below the glass transition temperature T_g of the substrate. At even higher pulse fluences where the T_g of the substrate might be reached this proposed mechanism may act in conjunction with the conventional mechanism, which is based on sinking of the NWs into a mushy post-T_g polymer.

Future work will aim to integrate thermo-mechanical models with this framework to quantitatively predict how much NW embedding occurs. Further, as NW embedding evolves the thermal interaction between the NWs and the polymer might change due to greater contact area between them. While this work has not accounted for this phenomenon future work will consider it.

Acknowledgments

This work was supported by the National Science Foundation USA [grants CMMI #1809289 and CBET # 1449383]; the Walmart Manufacturing Innovation Foundation; and the Oregon Nanoscience and Microtechnologies gap fund. The raw/processed data for this manuscript is available upon request.

ORCID iDs

Rajiv Malhotra https://orcid.org/0000-0003-4914-4497

References

[1] Sachse C, Weiß N, Gaponik N, Müller-Meskamp L, Eychmüller A and Leo K 2014 ITO-free, small-molecule organic solar cells on spray-coated copper-nanowire-based transparent electrodes *Adv. Energy Mater.* **4** 6

[2] Jiu J, Sugahara T, Nogi M, Araki T, Suganuma K, Uchida H and Shinozaki K 2013 High-intensity pulse light sintering of silver nanowire transparent films on polymer substrates: the effect of the thermal properties of substrates on the performance of silver films *Nanoscale* **5** 11820–8

[3] Perelaer J, Abbel R, Wünscher S, Jani R, van Lammeren T and Schubert Ulrich S 2012 Roll-to-roll compatible sintering of inkjet printed features by photonic and microwave exposure: from non-conductive ink to 40% bulk silver conductivity in less than 15 s *Adv. Mater.* **24** 2620–5

[4] Wan-Ho C, Hyun-Jun H, Seung-Hyun L and Hak-Sung K 2013 *In situ* monitoring of a flash light sintering process using silver nano-ink for producing flexible electronics *Nanotechnology* **24** 035202

[5] Hyun-Jun H, Wan-Ho C and Hak-Sung K 2012 *In situ* monitoring of flash-light sintering of copper nanoparticle ink for printed electronics *Nanotechnology* **23** 485205

[6] Sung-Jun J, Hyun-Jun H and Hak-Sung K 2014 Highly conductive copper nano/microparticles ink via flash light sintering for printed electronics *Nanotechnology* **25** 265601

[7] Myeong-Hyeon Y, Sung-Jun J and Hak-Sung K 2017 Multi-pulse flash light sintering of bimodal Cu nanoparticle-ink for highly conductive printed Cu electrodes *Nanotechnology* **28** 205205

[8] Hyun-Jun H, Soo-Chul L, Kyung-Chul O, Jin-Seong P and Hak-Sung K 2016 Photonic sintering via flash white light combined with deep UV and NIR for $SrTiO_3$ thin film vibration touch panel applications *Nanotechnology* **27** 505209

[9] Wan-Ho C, Yeon-Taek H, Seung-Hyun L and Hak-Sung K 2016 Electrical wire explosion process of copper/silver hybrid nano-particle ink and its sintering via flash white light to achieve high electrical conductivity *Nanotechnology* **27** 205704

[10] Chung W-H, Park S-H, Joo S-J and Kim H-S 2018 UV-assisted flash light welding process to fabricate silver nanowire/graphene on a PET substrate for transparent electrodes *Nano Res.* **11** 2190–203

[11] Jiu J, Nogi M, Sugahara T, Tokuno T, Araki T, Komoda N, Suganuma K, Uchida H and Shinozaki K 2012 Strongly adhesive and flexible transparent silver nanowire conductive films fabricated with a high-intensity pulsed light technique *J. Mater. Chem.* **22** 23561–7

[12] Mallikarjuna K, Hwang H-J, Chung W-H and Kim H-S 2016 Photonic welding of ultra-long copper nanowire network for flexible transparent electrodes using white flash light sintering *RSC Adv.* **6** 4770–9

[13] Song C-H, Han C J, Ju B-K and Kim J-W 2016 Photoenhanced patterning of metal nanowire networks for fabrication of ultraflexible transparent devices *ACS Appl. Mater. Interfaces* **8** 480–9

[14] Zhong Z, Woo K, Kim I, Hwang H, Kwon S, Choi Y-M, Lee Y, Lee T-M, Kim K and Moon J 2016 Roll-to-roll-compatible, flexible, transparent electrodes based on self-nanoembedded Cu nanowires using intense pulsed light irradiation *Nanoscale* **8** 8995–9003

[15] Dexter M, Gao Z, Bansal S, Chang C-H and Malhotra R 2018 Temperature, crystalline phase and influence of substrate properties in intense pulsed light sintering of copper sulfide nanoparticle thin films *Sci. Rep.* **8** 2201

[16] Park S-H, Chung W-H and Kim H-S 2014 Temperature changes of copper nanoparticle ink during flash light sintering *J. Mater. Process. Technol.* **214** 2730–8

[17] Dharmadasa R, Dharmadasa I M and Druffel T 2014 Intense pulsed light sintering of electrodeposited CdS thin films *Adv. Eng. Mater.* **16** 1351–61

[18] Bansal S and Malhotra R 2016 Nanoscale-shape-mediated coupling between temperature and densification in intense pulsed light sintering *Nanotechnology* **27** 495602

[19] MacNeill W, Choi C-H, Chang C-H and Malhotra R 2015 On the self-damping nature of densification in photonic sintering of nanoparticles *Sci. Rep.* **5** 14845

[20] Song C-H, Ok K-H, Lee C-J, Kim Y, Kwak M-G, Han C J, Kim N, Ju B-K and Kim J-W 2015 Intense-pulsed-light irradiation of Ag nanowire-based transparent electrodes for use in flexible organic light emitting diodes *Org. Electron.* **17** 208–15

[21] Zhang Y, Wen Y-H, Zheng J-C and Zhu Z-Z 2009 Energetic and structural evolution of gold nanowire under heating process: a molecular dynamics study *Phys. Lett.* A **373** 3454–8
[22] Parhami F and McMeeking R M 1998 A network model for initial stage sintering *Mech. Mater.* **27** 111–24
[23] Ding S *et al* 2016 One-step fabrication of stretchable copper nanowire conductors by a fast photonic sintering technique and its application in wearable devices *ACS Appl. Mater. Interfaces* **8** 6190–9
[24] Lü X, Shen W Z and Chu J H 2002 Size effect on the thermal conductivity of nanowires *J. Appl. Phys.* **91** 1542–52
[25] Slifkin L, Lazarus D and Tomizuka T 1952 Self-diffusion in pure polycrystalline silver *J. Appl. Phys.* **23** 1032–4
[26] Singman C N 1984 Atomic volume and allotropy of the elements *J. Chem. Educ.* **61** 137
[27] Nanda K K, Maisels A, Kruis F E, Fissan H and Stappert S 2003 Higher surface energy of free nanoparticles *Phys. Rev. Lett.* **91** 4
[28] Daw M S, Foiles S M and Baskes M I 1993 The embedded-atom method: a review of theory and applications *Mater. Sci. Rep.* **9** 251–310
[29] Williams P L, Mishin Y and Hamilton J C 2006 An embedded-atom potential for the Cu–Ag system *Modelling Simul. Mater. Sci. Eng.* **14** 817
[30] Zhang Y, Wu L, Guo X, Jung Y-G and Zhang J 2016 Molecular dynamics simulation of electrical resistivity in sintering process of nanoparticle silver inks *Comput. Mater. Sci.* **125** 105–9
[31] Lee P, Lee J, Lee H, Yeo J, Hong S, Nam Koo H, Lee D, Lee Seung S and Ko Seung H 2012 Highly stretchable and highly conductive metal electrode by very long metal nanowire percolation network *Adv. Mater.* **24** 3326–32
[32] Alarifi H A, Atis M, Ozdogan C, Hu A, Yavuz M and Zhou Y 2013 Molecular dynamics simulation of sintering and surface premelting of silver nanoparticles *Mater. Trans.* **54** 884–9
[33] Nair M T S and Nair P K 1989 Chemical bath deposition of CuxS thin films and their prospective large area applications *Semicond. Sci. Technol.* **4** 191–9
[34] Niittynen J, Sowade E, Kang H, Baumann R R and Mäntysalo M 2015 Comparison of laser and intense pulsed light sintering (IPL) for inkjet-printed copper nanoparticle layers *Sci. Rep.* **5** 10